



Robust α -Fe₂O₃@TiO₂ Core–Shell Structures With Tunable Buffer Chambers for High-Performance Lithium Storage

Chunyuan Pian¹, Weichao Peng², Haoyu Ren³, Chao Ma⁴, Yun Su¹, Ruixia Ti¹, Xiuyu Chen¹, Lixia Zhu¹, Jingjing Liu¹, Xinzhi Sun¹, Bin Wang^{1*}, Bingxuan Niu^{5*} and Dapeng Wu^{3,6*}

¹School of Physics and Electronic Engineering, Xinxiang University, Xinxiang, China, ²Key Laboratory for Biomedical Effects of Nanomaterials and Nanosafety, Institute of High Energy Physics, Chinese Academy of Sciences, Beijing, China, ³Collaborative Innovation Centre of Henan Province for Green Manufacturing of Fine Chemicals, Key Laboratory of Green Chemical Media and Reactions, Ministry of Education, School of Chemistry and Chemical Engineering, Henan Normal University, Xinxiang, China, ⁴School of Mechanical and Electrical Engineering, Xinxiang University, Xinxiang, China, ⁵College of Pharmacy, College of Biomedical Engineering, Xinxiang Medical University, Xinxiang, China, ⁶School of Environment, Henan Normal University, Xinxiang, China

OPEN ACCESS

Edited by:

Kewei Shu,
Shaanxi University of Science and
Technology, China

Reviewed by:

Hongsen Li,
Qingdao University, China
Yuxiang Hu,
The University of Queensland,
Australia

*Correspondence:

Bin Wang
wangbin2013@xxu.edu.cn
Bingxuan Niu
nbx@xxmu.edu.cn
Dapeng Wu
dpengwu@126.com

Specialty section:

This article was submitted to
Electrochemistry,
a section of the journal
Frontiers in Chemistry

Received: 31 January 2022

Accepted: 23 February 2022

Published: 07 April 2022

Citation:

Pian C, Peng W, Ren H, Ma C, Su Y,
Ti R, Chen X, Zhu L, Liu J, Sun X,
Wang B, Niu B and Wu D (2022)
Robust α -Fe₂O₃@TiO₂ Core–Shell
Structures With Tunable Buffer
Chambers for High-Performance
Lithium Storage.
Front. Chem. 10:866369.
doi: 10.3389/fchem.2022.866369

α -Fe₂O₃ has high potential energy storage capacity and can serve as a green and low-cost anode material for lithium-ion batteries. However, α -Fe₂O₃ suffers large volume expansion and pulverization. Based on DFT calculations, TiO₂ can effectively maintain the integrity of the crystal structure during the discharge/charge process. Well-defined cubic α -Fe₂O₃ is coated with a TiO₂ layer using the hydrothermal method with the assistance of oxalic acid surface treatment, and then α -Fe₂O₃@TiO₂ with tunable buffer chambers is obtained by altering the hydrochloric acid etching time. With the joint efforts of the buffer chamber and the robust structure of the TiO₂ layer, α -Fe₂O₃@TiO₂ alleviates the expansion of α -Fe₂O₃ during the discharge/charge process. The optimized sample (FT-1h) achieves good cycling performance. The reversible specific capacity remains at 893.7 mA h g⁻¹, and the Coulombic efficiency still reaches up to 98.47% after 150 cycles at a current density of 100 mA g⁻¹. Furthermore, the reversible specific capacity can return to 555.5 mA h g⁻¹ at 100 mA g⁻¹ after cycling at a high current density. Hence, the buffer chamber and the robust TiO₂ layer can effectively improve the cycling stability and rate performance of α -Fe₂O₃.

Keywords: α -Fe₂O₃@TiO₂, core-shell structures, tunable buffer chambers, cycle stability, lithium storage

INTRODUCTION

With the rapid development of portable electronic devices and electric vehicles, the demand for batteries with higher energy densities, greater safety, and longer cycling lifetimes has become extremely urgent (Duffner et al., 2021; Wang et al., 2022). Lithium-ion batteries (LIBs) have been widely used over the past few years and have been increasingly studied (Kim et al., 2019; Guo and Li, 2021). The ideal anode material should have a much higher cycle life and a moderate potential plateau (Jin et al., 2021). Transition metal oxides (MO_x, where M represents Fe, Co, Mn, Ni, etc.) are usually used as anode materials in lithium-ion batteries due to their high theoretical specific capacity (Li et al., 2021a; Li Q. et al., 2021). α -Fe₂O₃ has become a promising anode material for Li-ion

batteries due to its high theoretical capacity (1,007 mAh g⁻¹) and low cost (Kong et al., 2016). However, the poor conductivity and violent volume expansion of α -Fe₂O₃ during the discharge/charge process result in its poor rate and cycling performance as an anode material in Li-ion batteries. To overcome these problems, many researchers have expended considerable efforts to test potential solutions, such as various morphologies [porous quasi-clusters (Li Z. et al., 2019), porous nanotubes (Wang Z. et al., 2018), and one-dimensional mesoporous nanowires (Li et al., 2020)] and conductive carbon material coatings [graphene oxide (Zhang et al., 2019), carbon cloth (Narsimulu et al., 2019), N-doped carbon hybrids (Li et al., 2018), and spherical graphite (Yan et al., 2020)]. Although the rate and cycling performance of α -Fe₂O₃ have been improved, they have still not reached satisfactory levels.

TiO₂ is an essential member of the family of transition metal oxides, which are widely used in photocatalysis (Xu et al., 2017; Wang L. et al., 2018; Shi et al., 2018; Wang et al., 2019a; Wang et al., 2019b), solar cells (Wu et al., 2017), and lithium-ion batteries (Huo et al., 2021). As an anode of lithium-ion batteries, TiO₂ has good cycling stability and a low volume expansion ratio (less than 4%) (Liang et al., 2020). However, the reversible capacity of TiO₂ as an anode material in lithium-ion batteries is low, and its theoretical capacity is only 335 mA h g⁻¹ (Liang et al., 2020). To improve the specific capacity of TiO₂, a large number of scientific researchers investigated different structures of TiO₂, such as porous (Nong et al., 2020), hollow nanosphere (Fan et al., 2021), branch-like (Gao et al., 2019), heterogeneous mesoporous hollow nanocage-in-nanocage, and sandwich structures (Yuan et al., 2019). Additionally, many attempts to combine carbon with TiO₂ have been made (Ni et al., 2019; Yuan et al., 2021). However, the specific capacity of TiO₂ has still not been significantly improved.

The combination of α -Fe₂O₃ and TiO₂ may form a new kind of Li-ion battery anode material. α -Fe₂O₃ grains grafted onto TiO₂/carbon nanofibers (CNFs) have been successfully fabricated by electrospinning and vapor–solid reaction (VSR), with the resulting material demonstrating greatly enhanced diffusion kinetics and structural stability for use in lithium-ion batteries (Yang et al., 2019). Robust Fe₂O₃ nanoplates have been coated with small TiO₂ nanoplates, forming a slice-on-slice structure with large voids, with the resulting material exhibiting good Li storage properties (Zhao et al., 2018). A bio-inspired nanotubular TiO₂/Fe₂O₃ composite has been fabricated by using a natural cellulose substance (laboratory filter paper) as the structural scaffold, showing good cycling stability and excellent rate capability (Li S. et al., 2019). Notably, a core–shell structure is an effective means to improve cycling performance (Li et al., 2021). Thus, α -Fe₂O₃@TiO₂ composed of a hollow inner core and an outer shell with massive mesopores has been prepared, thus exhibiting outstanding electrochemical properties (Fu et al., 2015).

Different from the aforementioned materials, a tunable buffer chamber is fabricated in this study. Cubic α -Fe₂O₃ is used as the core, and a TiO₂ layer is coated on this core using the hydrothermal method. With an increasing etching time, α -Fe₂O₃@TiO₂ becomes more hollowed out. Thus, a buffer chamber is formed between α -Fe₂O₃ and TiO₂. With the help

of this structure, the volume expansion of α -Fe₂O₃ during the discharge/charge process is alleviated when applied as the anode material in lithium-ion batteries, which is also proven by theoretical calculations.

THEORETICAL AND EXPERIMENTAL METHOD

Calculation Method

With the density functional theory (DFT) (Hohenberg, 1964; Kohn and Sham, 1965), the process of Li-ion de/insertion in α -Fe₂O₃ and TiO₂ is studied. Ultrasoft pseudopotentials were used to calculate the interaction of the ionic core and valence electrons for Fe 3d⁶4s², Ti 3s²3p⁶3d²4s², Li 1s²2s¹, and O 2s²2p⁴. The exchange and correlation terms were described with the generalized gradient approximation (GGA) of Perdew–Burke–Ernzerhof (PBE) (Perdew et al., 1996; Perdew et al., 1998). Monkhorst–Pack k-point meshes were conducted to address the Brillouin-zone integrations (Monkhorst and Pack, 1976). Convergence criteria were set as follows: the maximum force, the maximum stress, and the maximum displacement on the atom were below 0.1 eV nm⁻¹, 0.02 GPa, and 5.0 × 10⁻⁵ nm, respectively.

A periodic structure was adopted in the calculation. The unit cells of α -Fe₂O₃ and anatase TiO₂ (space group of R-3C and 141/AMD) contained 12 iron atoms, 18 oxygen atoms, four titanium atoms, and eight oxygen atoms (**Supplementary Figure S1**). Moreover, 380 eV was set as the cutoff energy for both. The number of k-points was set as 6 × 6 × 2 and 7 × 7 × 3. The calculated lattices agreed well with the theoretical and experimental data (Finger and Hazen, 1980; Arlt et al., 2000; Zhang et al., 2017; Jenness et al., 2018) (**Supplementary Table S1**).

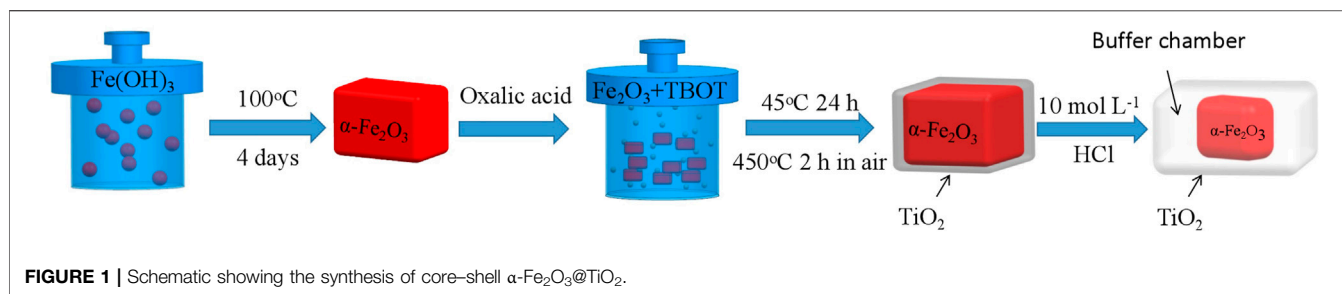
Synthesis of α -Fe₂O₃

With vigorous stirring in an oil bath at 75°C, 50 ml of 2.0 mol/L FeCl₃·6H₂O solution was added to a round-bottom flask containing 50 ml of 5.4 mol/L NaOH. After stirring for 5 min, a red-brown Fe(OH)₃ colloid formed in the flask, which was then transferred to a high-temperature and high-pressure PTFE reactor. The hydrothermal reaction was conducted at 100°C for 4 h. After cooling to room temperature, the obtained red precipitate was centrifuged, successively rinsed with deionized water and ethanol three times, and then dried overnight to obtain α -Fe₂O₃.

The synthesized α -Fe₂O₃ was treated with oxalic acid, for which 8 ml of deionized water was added to a beaker containing 0.2 g of α -Fe₂O₃, and then 0.1 g of oxalic acid was added. After shaking at room temperature for 6 h, the red precipitate was obtained by centrifugation and then successively rinsed with deionized water and ethanol three times. After drying overnight, oxalic acid-treated α -Fe₂O₃ was obtained.

Synthesis of Core–Shell α -Fe₂O₃@TiO₂

The core–shell α -Fe₂O₃@TiO₂ synthesis process is illustrated in **Figure 1**. In a beaker containing 33 ml of absolute ethanol, 0.1 g of oxalic acid-treated α -Fe₂O₃ was added, and then, 0.1 ml of



concentrated ammonia water was added with stirring and stirred for 5 min. Next, 0.25 ml of tetrabutyl titanate (TBOT) was added with vigorous stirring, and ultrasonication was performed for 40 min. The solution in the beaker was transferred to the PTFE reactor. After hydrothermal reaction at 45°C for 24 h, the solution was cooled to room temperature and then centrifuged. The red precipitate was rinsed with deionized water and ethanol three times and then dried overnight. In an air environment, the product was calcined at 450°C for 2 h to obtain $\alpha\text{-Fe}_2\text{O}_3\text{@TiO}_2$, and then, 0.1 g $\alpha\text{-Fe}_2\text{O}_3\text{@TiO}_2$ was added to 25 ml of 10 mol/L HCl and oscillated for 0.5, 1, 2, 4, and 12 h. Then, they were successively rinsed with deionized water and ethanol three times and dried overnight to obtain $\alpha\text{-Fe}_2\text{O}_3\text{@TiO}_2$ at different etching degrees. The samples were denoted as FT-0.5h, FT-1h, FT-2h, FT-4h, and FT-12h (pure TiO_2).

Material Characterization

X-ray diffraction (XRD, Bruker D8, Germany) was used to characterize the synthesized powder samples. The morphology of each sample was observed by field emission scanning electron microscopy (FESEM) and high-resolution transmission electron microscopy (HRTEM, JEOL, JSM-2100, Japan). The component and valence analysis of the synthesized samples were carried out by X-ray photoelectron spectroscopy (XPS, ESCALAB 250, an Al K excitation source, United States). Additionally, HRTEM (TF20, JOEL, 2100F, Japan) was used to map the elemental distribution of the samples. The specific surface area and pore size analyzer (BET, ASI Q Mini QUANTACHROME) was used to determine the porosity of the samples.

Electrochemical Characterization

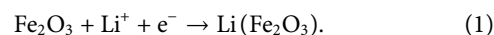
The prepared samples were mixed with acetylene black and polyvinylidene fluoride (PVDF) at a weight ratio of 7:2:1 in N-methyl-2 pyrrolidone (NMP). The obtained slurry was uniformly smeared on a 9- μm -thick copper foil and dried in a vacuum oven at 80°C for 10 h, and then a 12-mm-diameter negative plate was cut, and 1 M LiPF_6 in a mixture of 1:1:1 vol.% ethylene carbonate (EC), diethyl carbonate (DEC), and dimethyl carbonate (DC) was used as the electrolyte (ternary electrolyte LBC305-1, Shenzhen Kejinzida Technology Co., Ltd.). With a 15.6-mm \times 0.45-mm lithium sheet as the positive electrode and a Celgard 2325 diaphragm as the battery separator, the prepared negative electrode was assembled into a CR2025 battery in a glove box (Super, Germany Mikrouna) that was filled with argon gas (water concentration <0.1 ppm and oxygen concentration <0.1 ppm). The cycling and rate

performance were tested with a Blue Power instrument (Wuhan Blue Electronics Co., Ltd.). An electrochemical workstation (Shanghai Chenhua Instrument Co., Ltd.) was used to obtain cyclic voltammetry (CV) curves, and a different electrochemical workstation (ZAHNER Company, Germany) was used to conduct electrochemical impedance spectroscopy (EIS).

RESULTS AND DISCUSSION

Calculation Analysis

According to the symmetry of $\alpha\text{-Fe}_2\text{O}_3$ and anatase TiO_2 , there are one and two symmetrical positions for Li ions to be inserted into $\alpha\text{-Fe}_2\text{O}_3$ (6b) and TiO_2 (16 h, 8 days), respectively (**Figure 2**). One unit cell of $\alpha\text{-Fe}_2\text{O}_3$ can accommodate six Li ions, but one unit cell of TiO_2 can only accommodate four Li ions. Thus, the reaction equation of Li ions and Fe_2O_3 is as follows:



Eq (1) is consistent with Yang et al. (2019). The reaction process of Li ions and TiO_2 is given in **Eq. 2**:



From **Eq. 2**, the theoretical capacity of TiO_2 can be calculated (335 mA h g^{-1}), which is consistent with Liang et al. (2020). After six Li ions were inserted into the $\alpha\text{-Fe}_2\text{O}_3$ unit cell, the volume expanded by 9.64%. The volume of TiO_2 expanded by 1.15% after four Li ions were inserted. Moreover, the one, two, three, four, and five and one, two, and three Li ions inserted in the cells at the different sites of $\alpha\text{-Fe}_2\text{O}_3$ and TiO_2 were also calculated (**Supplementary Table S2**). With an increasing number of Li ions inserted in the $\alpha\text{-Fe}_2\text{O}_3$ cell, the volume continued to expand. However, it was amazing to find that the expansion rate of TiO_2 always remained below 2.2%. With the same number of Li ions inserted in the cell, the volume expansion of $\alpha\text{-Fe}_2\text{O}_3$ was larger than that of TiO_2 . There are two reasons for this result: one is that the interstitial vacancy (8 days and 16 h) of TiO_2 is larger than that of $\alpha\text{-Fe}_2\text{O}_3$ (6b) and the other is that with Li ions insertion, the angle of Ti-O-Ti (**Figures 2C,D**) changes from 155.148° to 179.022°, which acts as a buffer. Hence, TiO_2 can effectively maintain its cell structure. Furthermore, it is believed that with an increasing number of Li ions inserted in $\alpha\text{-Fe}_2\text{O}_3$ and the combination of O ions, the cell will continue to expand. This mechanism is the reason to coat $\alpha\text{-Fe}_2\text{O}_3$ with TiO_2 . Moreover, it

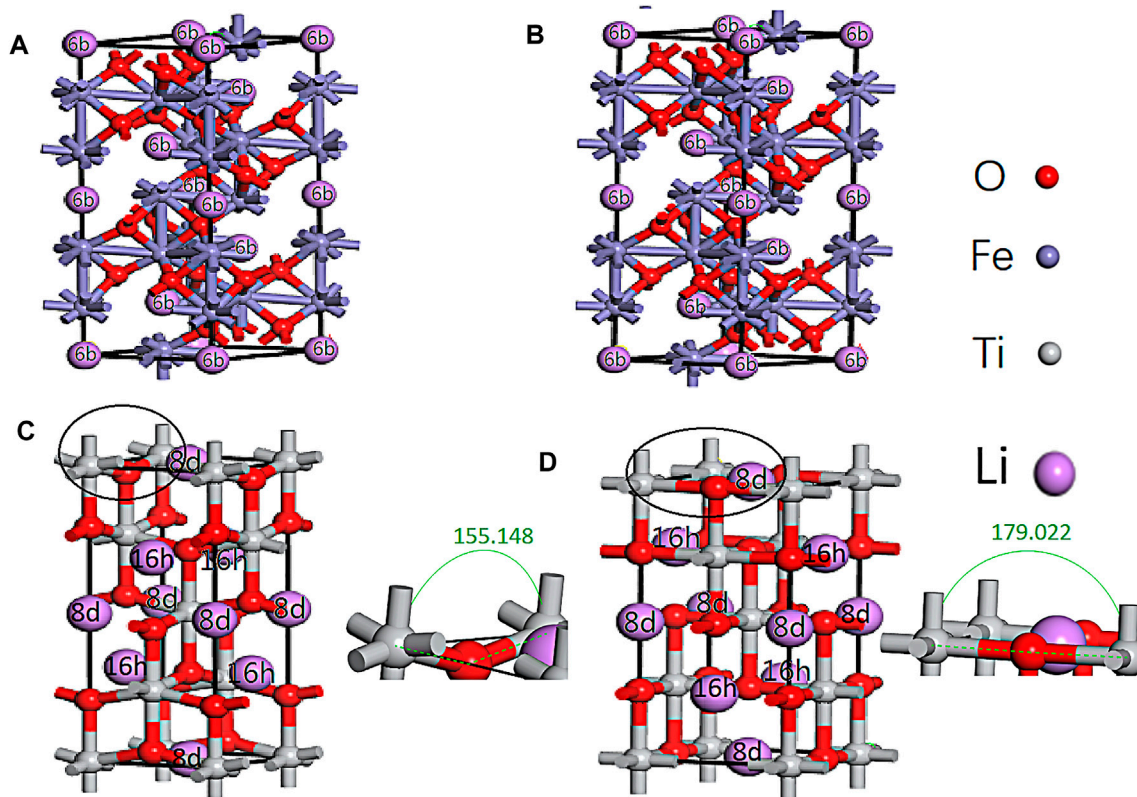


FIGURE 2 | Li inserted in the symmetrical sites of $\alpha\text{-Fe}_2\text{O}_3$ (6b) and TiO_2 (16h, 8 days) before the geometry optimization (A,B) and after the geometry optimization (B,D).

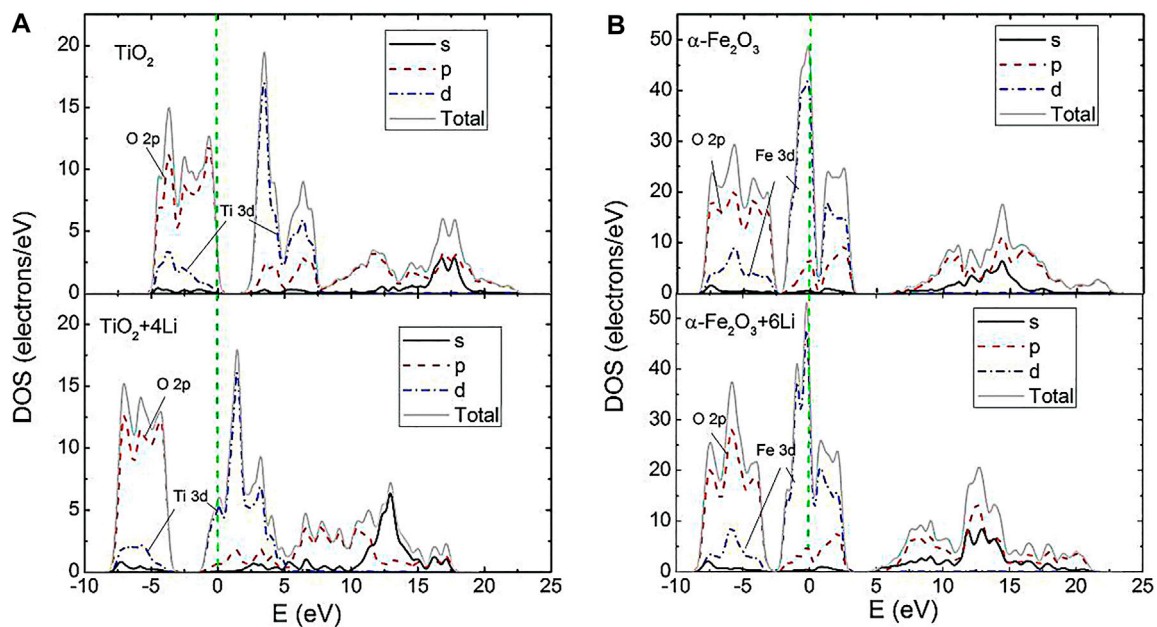


FIGURE 3 | Density of states of TiO_2 (A) and $\alpha\text{-Fe}_2\text{O}_3$ (B) with and without Li inserted at the symmetrical sites. The green dashed line represents a Fermi energy of 0.

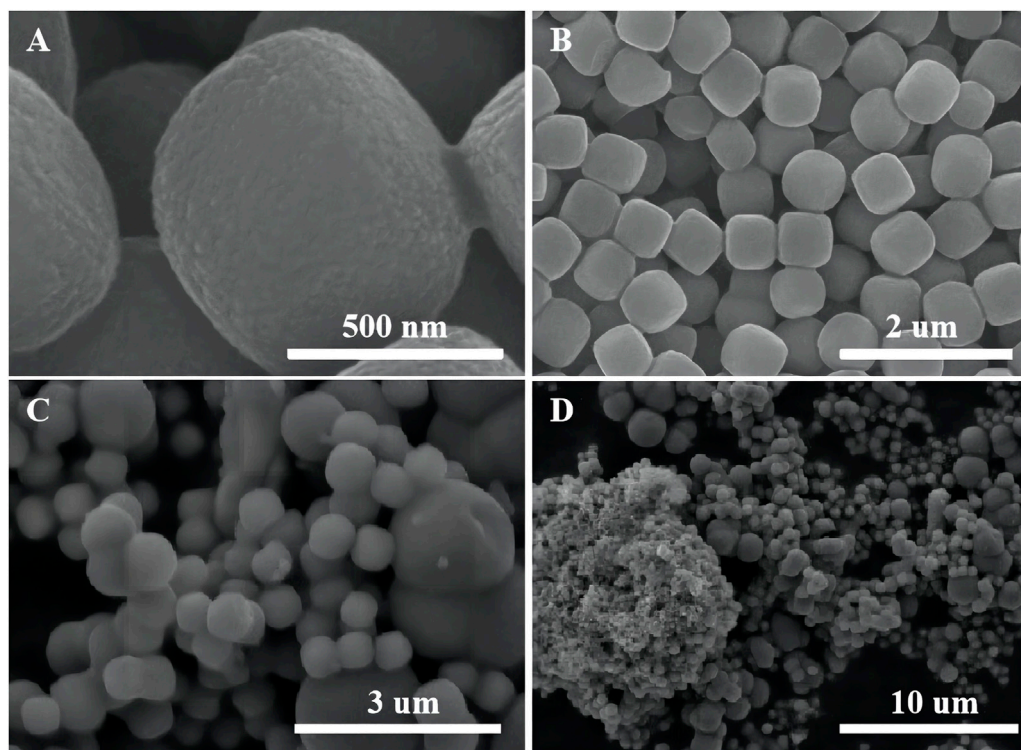


FIGURE 4 | SEM images of α -Fe₂O₃ (A) and (B) and unprocessed α -Fe₂O₃ coated with TiO₂ (C) and (D).

is not found that the bonds of Ti-O and Fe-O are broken, which can be verified from **Figure 2**, the population analysis (**Supplementary Table S3**), and the density of states (DOS) (**Figure 3**).

The electronic population is usually used to assess the covalent or ionic nature of a bond. A high value of the bond population expresses a strong covalent bond (Aouadi, 2006). Both α -Fe₂O₃ and TiO₂ have two types of bonds, which are marked I and II in **Supplementary Figure S1**. From **Supplementary Table S3**, it can be found that the electronic populations of Fe-O I were little larger than those of Fe-O II. Meanwhile, the bond length of Fe-O I was shorter than that of Fe-O II. Nevertheless, the electronic population of Ti-O I was larger than that of Ti-O II, which means Ti-O I had stronger covalent bonds. When Li ions were inserted in α -Fe₂O₃ and TiO₂, the electronic population and bond length increased. Bond length increase can be attributed to volume expansion. Among them, the electronic population of Ti-O I increased the most, which means Ti-O I was enhanced. Instead of breaking, Ti-O I was strengthened.

The DOS of α -Fe₂O₃ and TiO₂ express two main regions near the Fermi level (**Figure 3**). The more important part is the first region, which is predominantly formed by non-metal O 2p states and Ti 3d (Fe 3d) states located between -10 and 0 eV. This part forms a strong p-d covalent bonding. With the Ti (Fe) and O atoms getting squeezed, it is found that the DOS below the Fermi level move to the low-energy part (the DOS of TiO₂+4 Li and Fe₂O₃+6 Li), which shows that Ti-O and Fe-O are enhanced. Furthermore, the TiO₂+4 Li DOS move more than the Fe₂O₃+6 Li

DOS. This result indicates that Ti-O is more enhanced, which agrees well with the electronic population analysis.

Morphological and Structural Characterization

The SEM images of α -Fe₂O₃ without coating TiO₂ are shown in **Figures 4A,B**. α -Fe₂O₃ is successfully synthesized during the experiment. The XRD result is consistent with the diffraction peak of α -Fe₂O₃ (Haematite, syn) in PDF#33-0664 (**Supplementary Figure S2**). α -Fe₂O₃ has a cubic morphology with relatively smooth surfaces and a size of approximately 400–500 nm. In order to compare the effect of oxalic acid-treated and untreated α -Fe₂O₃ coating with TiO₂, untreated α -Fe₂O₃ is used for TiO₂ layer cladding. According to **Figures 4C,D**, when untreated α -Fe₂O₃ is coated with TiO₂, it is more prone to heterogeneous nucleation, and agglomeration is easy to occur. After cladding, the homogeneous Fe₂O₃ particles become inhomogeneous α -Fe₂O₃@TiO₂ particles.

Figure 5 shows the samples of oxalic acid-treated α -Fe₂O₃ coated with TiO₂ and etched for different periods of time. Clearly, with an increasing etching time, α -Fe₂O₃@TiO₂ gradually changes from a core-shell structure to a completely hollowed out TiO₂ structure. The average core-shell sizes of different samples are listed in **Supplementary Table S4**. With hydrochloric acid etching, the thickness of shell changes a little, reducing from 58 to 45 nm, and maintains at 53 nm during the etching time of 1–4 h, while the core size changes

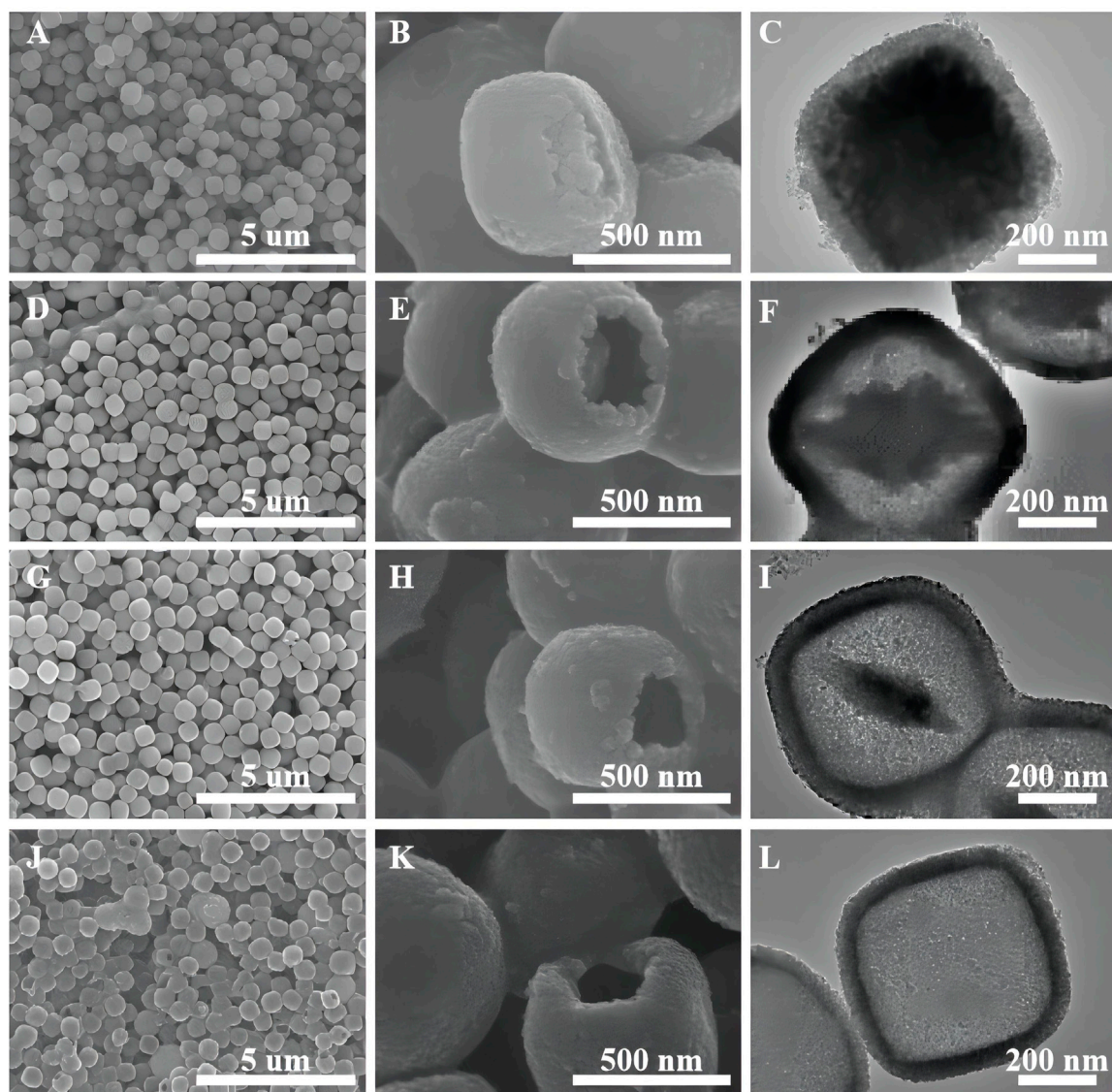


FIGURE 5 | SEM images of oxalic acid-treated α - Fe_2O_3 coated with TiO_2 and etched for different periods of time [FT-0.5h (A,B), FT-2h (D,E), FT-4h (G,H), and FT-12h (J,K) (pure TiO_2)]. TEM images of oxalic acid-treated α - Fe_2O_3 coated with TiO_2 and etched for different periods of time [FT-0.5h (C), FT-2h (F), FT-4h and (I), FT-12h (L) (pure TiO_2)].

greatly. The vertical diagonal (diagonal 1) changes from 560 to 100 nm. The horizontal diagonal (diagonal 2) changes from 568 to 419 nm. Thus, hydrochloric acid etching mainly aims to Fe_2O_3 .

As shown in **Figure 6**, the sample etched for 1 h (FT-1h) possesses a well-defined core-shell structure with a buffer chamber between the α - Fe_2O_3 core and the TiO_2 shell. From **Figure 6A**, it can be clearly observed that TiO_2 is successfully coated on α - Fe_2O_3 . Furthermore, the TiO_2 coating layers are very uniform with few ruptures (**Figure 6B**). In addition, **Figure 6C** shows that there is a chamber between the α - Fe_2O_3 core and the TiO_2 shell whose thickness is about 80 nm. According to the EDS mapping of a single α - Fe_2O_3 @ TiO_2 core-shell structure (**Figure 6D**), Fe, Ti, and O are evenly distributed. The red

section in **Figure 6E** shows that the TiO_2 layer covers the surface of α - Fe_2O_3 @ TiO_2 , and the yellow part in **Figure 6F** represents the α - Fe_2O_3 core structure. The green section illustrated in **Figure 6G** refers to O that is jointly contained by α - Fe_2O_3 and the TiO_2 covering layer in a single α - Fe_2O_3 @ TiO_2 core-shell structure. The composition of composite is further demonstrated by energy-dispersive spectroscopy (EDS), shown in **Figure 6H**. From the illustration, it shows that the compound is mainly composed of Fe_2O_3 and TiO_2 , and Fe_2O_3 is the main part. **Figure 7** displays the HRTEM image of FT-1h α - Fe_2O_3 @ TiO_2 . The stripes and grids on dark and light are different, which demonstrated that they were assembled by small crystals with measured lattice d-spacings of 0.35 and 0.37 nm, corresponding to the (101) plane of anatase TiO_2 and the (012) plane of Fe_2O_3 ,

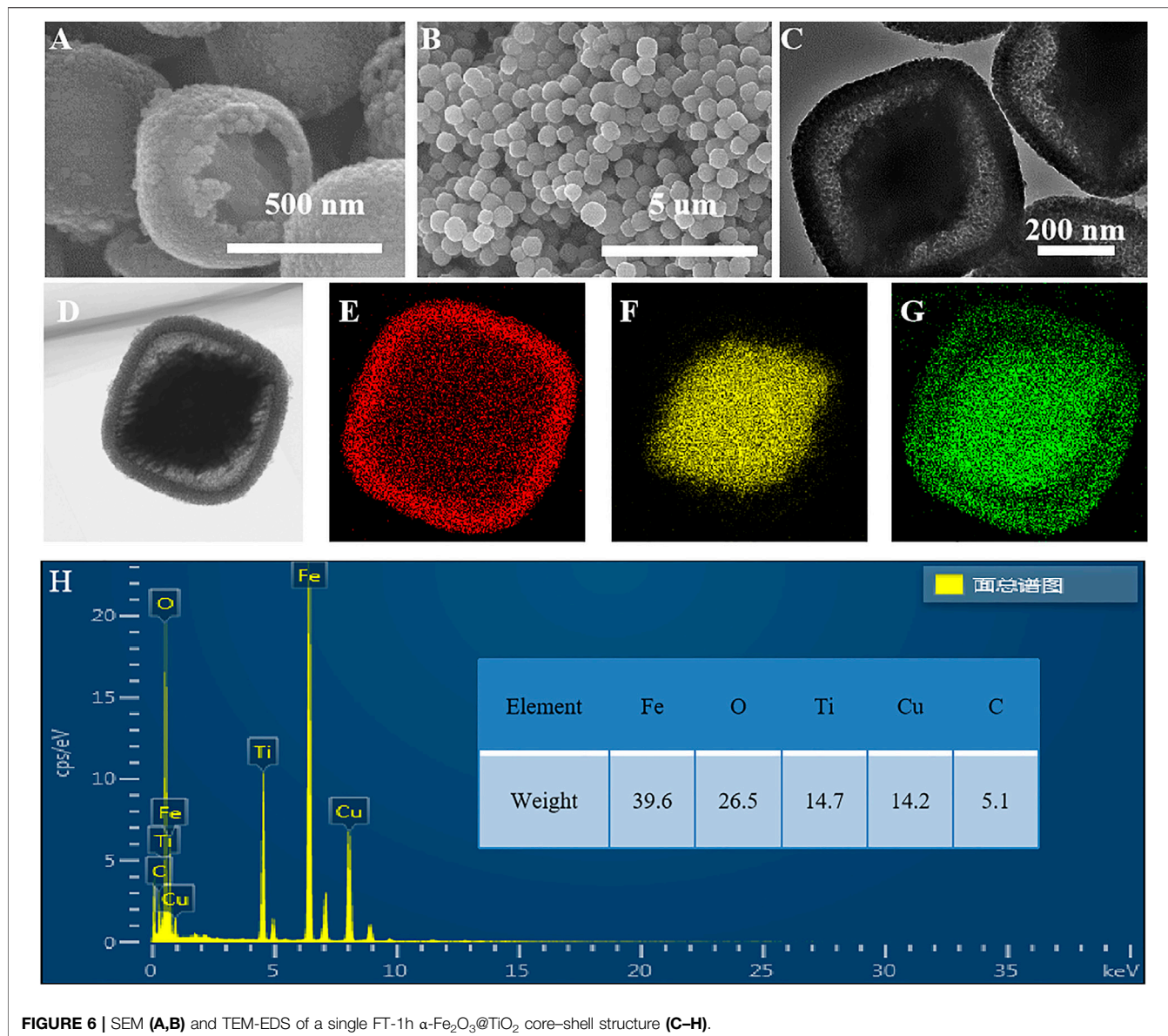
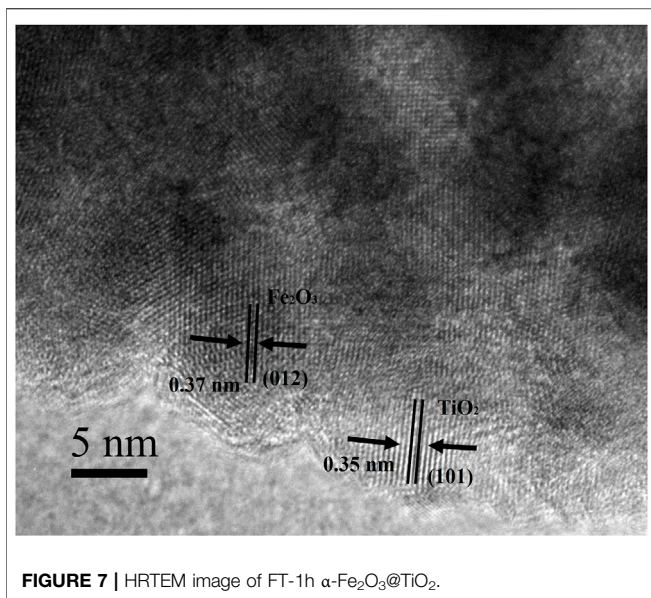


FIGURE 6 | SEM (A,B) and TEM-EDS of a single FT-1h α -Fe₂O₃@TiO₂ core-shell structure (C-H).

respectively. So, it can be proven that TiO₂ is uniformly dispersed on the surface of Fe₂O₃.

The chemical composition and crystal phase of the samples were investigated by XRD analysis. **Figure 8** shows that the diffraction peak $2\theta = 25.28^\circ, 37.8^\circ, 48.05^\circ, 55.06^\circ,$ and 62.69° corresponds to the (101), (004), (200), (211), and (204) planes of TiO₂, which is consistent with PDF#21-1272 (the diffraction peak of anatase). Samples FT-0.5h, FT-1h, FT-2h, and FT-4h present the characteristic peaks of Fe₂O₃ and TiO₂, which expressed that TiO₂ coating is successfully combined with α -Fe₂O₃. Furthermore, it can be observed that the intensity of the characteristic peak at 24.1° of α -Fe₂O₃ decreases, and the characteristic peak at 25.3° of TiO₂ increases with an increasing etching time. In addition, no additional peaks were observed, suggesting high purity of the samples, which shows good agreement with the results of XPS spectra (**Figure 9**).

The XPS characterization was conducted to examine the chemical composition of samples (FT-0.5h, FT-1h, FT-2h, FT-4h, and FT-12h (pure TiO₂)). The complete survey spectrum (**Figure 9A**) of α -Fe₂O₃@TiO₂ samples (FT-0.5h, FT-1h, FT-2h, and FT-4h) reveal the existence of Ti, Fe, and O elements. For the C 1s XPS spectrum, the peak at 285.00 eV is attributed to adventitious carbon (Zhong et al., 2017; Yang et al., 2019). The high-resolution XPS spectrum of Fe 2p was composed of two distinct peaks at 710.90 and 724.40 eV (**Figure 9B**), which correspond to Fe 2p^{2/3} and 2p^{1/2} with satellite lines. The spectrum is consistent with the characteristic of Fe³⁺ α -Fe₂O₃ (Zhong et al., 2017; Yang et al., 2019). In the spectrum of Ti 2p (**Figure 9C**), the Ti 2p^{3/2} and Ti 2p^{1/2} peaks were located at binding energies of 458.70 and 464.65 eV, respectively, which is in agreement with the value of Ti⁴⁺ in the TiO₂ lattice (Zhong et al., 2017; Zhao et al., 2018). The spectrum of the O1s core level is shown in **Figure 9D**,



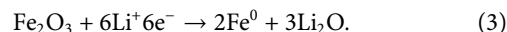
where binding energy peaks at 531.80 eV originate from bonded hydroxyl groups (Yang et al., 2019). For the broad peak centered at 530.00 eV, it is attributed to metal-bonding in both oxides (Zhao et al., 2018; Yang et al., 2019).

The texture characteristic of α -Fe₂O₃@TiO₂ was further confirmed by N₂ adsorption/desorption isotherm, as shown in **Figure 10**. It can be observed from **Figure 10A** that the specific surface area of pure α -Fe₂O₃ was very small, only 2.07 m² g⁻¹. After coating with TiO₂, the specific surface area increased to approximately 30 m² g⁻¹, and that is because pure α -Fe₂O₃ is smoother and denser than TiO₂, which can be seen from **Figure 4**. The surface bulge of TiO₂ was more obvious than that of pure α -Fe₂O₃. After etching for 0.5, 1, 2, 4, and 12 h (pure TiO₂), more pores formed. The specific surface area increased to 32.1, 34.39, 36.96, 43.845, and 131.91 m² g⁻¹. The isotherms were identified as IUPAC type IV, which is characteristic of mesoporous materials. The pore size distribution obtained from the isotherm indicates a number of pores 4–8 nm in the samples (**Figure 10B**). With increasing etching time, the pore volume increases. A structure with abundant mesopores is likely to buffer the volume expansion and allow the penetration of electrolyte for complete contact with the active material, thus playing an important role in improving the electrochemical properties of α -Fe₂O₃@TiO₂.

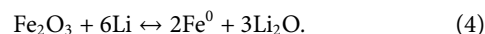
Cyclic Voltammetry and Galvanostatic Cycling

Electrochemical performances of α -Fe₂O₃@TiO₂ (FT-1h) were investigated as anode materials for LIBs to demonstrate the effectiveness in improving lithium storage. **Figure 11A** shows the first four CV curves of the FT-1h sample between 0.01 and 3 V at a scan rate of 0.1 mV⁻¹. It can be observed that the sample has a reduction peak and an oxidation peak at a potential of 1.73/2.13 V, which may be attributed to the de/insertion of lithium ions from TiO₂, as shown in **Eq. 2**. There are two oxidation peaks

at potentials of 0.92 and 1.12 V, which correspond to the lithium reaction of Fe₂O₃, respectively, as shown in **Eq. 3** (Fu et al., 2015).

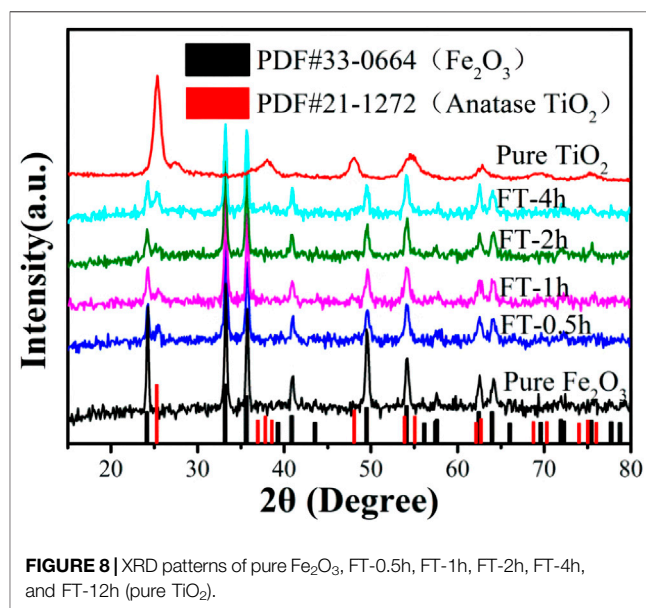


In addition, the oxidation peak between 1.5 and 2.0 V may correspond to Fe⁰ being reoxidized to Fe₂O₃, as shown in **Eq. 4** (Fu et al., 2015).



After the second charge–discharge cycle, the peak position slightly shifts, and the peak strength slightly weakens, which may be attributed to the polarization of the anode material and the formation of an SEI film during the charge–discharge process (Fu et al., 2015). It can be clearly observed that the curves of the fourth charge–discharge cycle and the third charge–discharge cycle coincide well, indicating that the FT-1h sample has good cycling stability.

Charge and discharge curves of the sample FT-1h with a voltage of 0.01–3 V are shown in **Figure 11B**. According to the previous analysis, a wide slope from 1.75 to 0.8 V is attributed to the Li⁺ intercalation into the crystal structure of α -Fe₂O₃ and the phase transformation from hexagonal to cubic Li₂Fe₂O₃ (Qin et al., 2018). Last, an obvious plateau at 0.8 V is ascribed to the reduction from Fe²⁺ into Fe⁰, and the formation of amorphous Li₂O and an SEI layer (Zhu et al., 2020). After the first charge and discharge cycle, the discharge/charge specific capacities of the FT-1h sample are 1,609.3 mA h g⁻¹ and 1,021.6 mA h g⁻¹, respectively. In the second process, a plateau at 1.0 V is observed, which agrees well with **Eq. 3**. Furthermore, the discharge specific capacity is reduced to 1,228.6 mA h g⁻¹, and the Coulombic efficiency is 99.1%. The fifth circle is similar to the second, except the length of the plateau, which is shorter than the one in the first circle, and this is due to the irreversible capacity loss derived from the formation amorphous Li₂O (Yang et al., 2019). The discharge specific capacity is



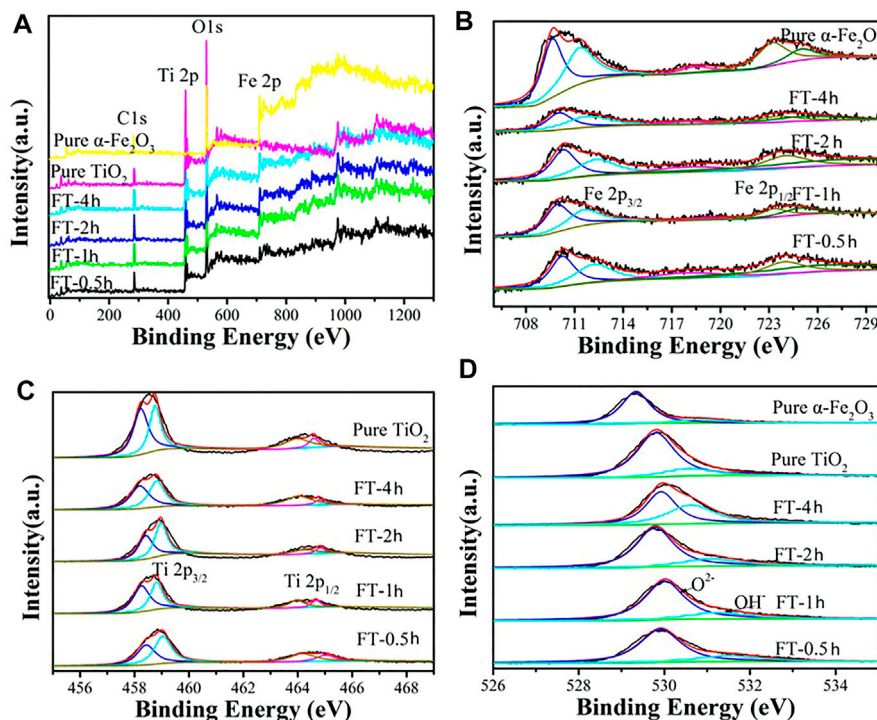


FIGURE 9 | XPS spectra of oxalic acid-treated $\alpha\text{-Fe}_2\text{O}_3$ coated with TiO_2 and etched for different periods of time [FT-0.5h, FT-1h, FT-2h, FT-4h, and FT-12h (pure TiO_2)]: (A) survey, (B) Fe2p, (C) Ti2p, and (D) O1s.

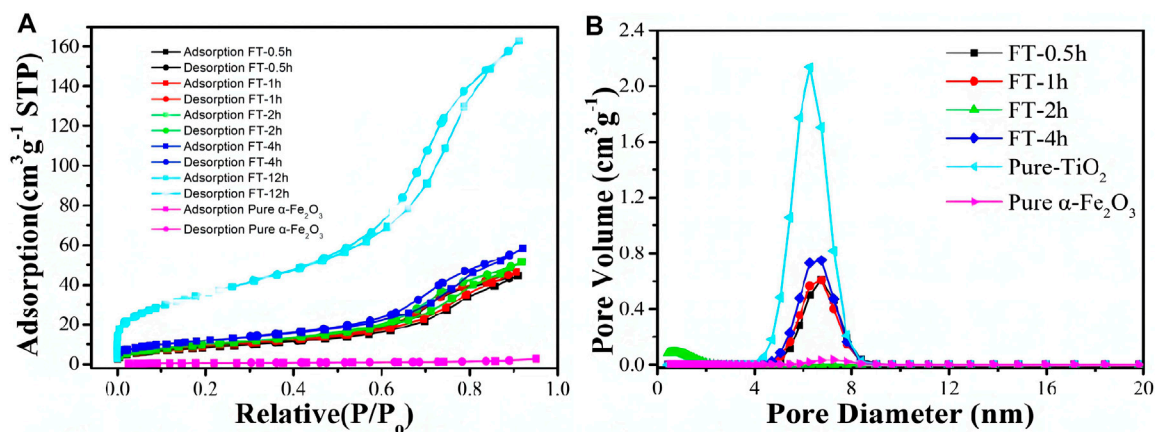


FIGURE 10 | BET figures (A) and pore size distribution (B) of oxalic acid-treated $\alpha\text{-Fe}_2\text{O}_3$ coated with TiO_2 and etched for different periods of time [pure $\alpha\text{-Fe}_2\text{O}_3$, FT-0.5h, FT-1h, FT-2h, FT-4h, and FT-12h (pure TiO_2)].

999.4 mA h g^{-1} after the fifth cycle. The 55th, 100th, and 150th curves express the similar circle curves, whose plateau is at 0.9 V, which is consistent with Eq. 3. After 150 charge–discharge cycles at a current density of 100 mA g^{-1} , the reversible capacity remains at $893.7 \text{ mA h g}^{-1}$, and the Coulombic efficiency is 98.4%.

Rate measurements of pure $\alpha\text{-Fe}_2\text{O}_3$, oxalic acid-treated $\alpha\text{-Fe}_2\text{O}_3$ coated with TiO_2 and etched for different periods of time

(FT-0.5h, FT-1h, FT-2h, FT-4h, and FT-12h (pure TiO_2)), and the charge–discharge tests at a current density of 100 mA g^{-1} for each cell after the rate performance test are shown in Figure 11C. The reversible capacities of FT-1h at current densities of 100 mA g^{-1} , 200 mA g^{-1} , 500 mA g^{-1} , 1 A g^{-1} , and 2 A g^{-1} reach 1,489.3, 586.8, 438.7, 332.7, and $224.5 \text{ mA h g}^{-1}$, respectively. When the current density is returned to 100 mA g^{-1} , the reversible capacity is still maintained at $555.5 \text{ mA h g}^{-1}$. After 100 charge–discharge

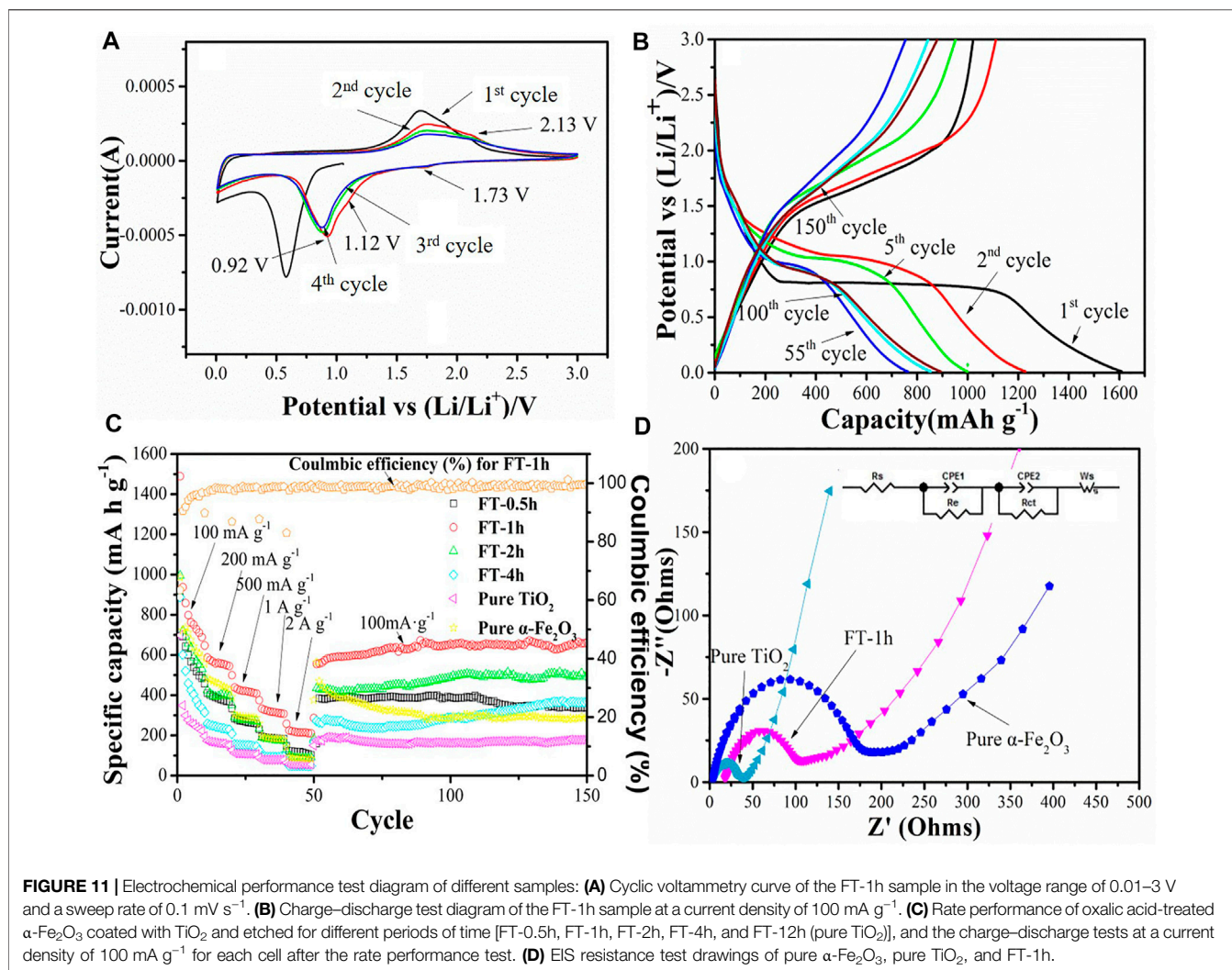


TABLE 1 | List of the reported works on Fe₂O₃@TiO₂ as anodes for lithium-ion batteries.

Material	Capacity/constant current density	Cycles	Ref.
Two-dimensional Fe ₂ O ₃ /TiO ₂ composite nanoplates	646 mA h g ⁻¹ /1,000 mA g ⁻¹	1,000 cycles	Qu et al. (2020)
Clustered Fe ₂ O ₃ /TiO ₂ composite	792 mA h g ⁻¹ /1,000 mA g ⁻¹	600 cycles	Chen et al. (2020)
TiO ₂ /Fe ₂ O ₃ nanotubular composite	571 mA h g ⁻¹ /100 mA g ⁻¹	150 cycles	Li et al. (2019a)
Fe ₂ O ₃ and TiO ₂ nanograins anchored on rGO layers	790 mA h g ⁻¹ /100 mA g ⁻¹	150 cycles	Kaprans et al. (2018)
α-Fe ₂ O ₃ /TiO ₂ composite	638 mA h g ⁻¹ /33.5 mA g ⁻¹	30 cycles	Qi et al. (2018)
Fe ₂ O ₃ @TiO ₂ core–shell nanospheres	497 mA h g ⁻¹ /100 mA g ⁻¹	100 cycles	Qin et al. (2018)
α-Fe ₂ O ₃ @TiO ₂ core–shell structures with tunable buffer chambers	893.7 mA h g ⁻¹ /100 mA g ⁻¹	150 cycles	This work

cycles at a current density of 100 mA g⁻¹, the reversible capacity remains at 682.0 mA h g⁻¹, and the Coulombic efficiency is 99.7%. During the long cycle, the Coulombic efficiency is maintained above 98%. The capacity decreases at the beginning and continuously increases during the latter long term cycle test. It is supposed to be the grain boundaries of iron metal and Li₂O formed in the electrochemical process (Eq. 4), which contributes to the extra energy storage of the composite (Li S. et al.,

2019). This phenomenon is common for most MO_x (M = Fe, Co, and Ni) attributed to the activation of the materials (Kaprans et al., 2018). Comparing the different etching times, it can be found that the battery performances of the etched samples are higher than that of pure α-Fe₂O₃ and TiO₂, indicating that the different degrees of buffer chambers can relieve, to a certain extent, the volume expansion of α-Fe₂O₃ during the discharge/charge process. Furthermore, the SEM images of pure Fe₂O₃ and FT-1h after

100 charge–discharge cycles are shown in **Supplementary Figure S3**. Fe_2O_3 morphology gets damaged severely if TiO_2 is not protected. On the contrary, sample FT-1h maintained the original morphology, which proved again that TiO_2 can effectively inhibit the volume expansion. Among the etched samples, FT-1h possesses the best performance. **Figure 11C** shows that FT-1h still has good cycling performance after the large rate performance test, while the reversible capacities of pure $\alpha\text{-Fe}_2\text{O}_3$ and pure TiO_2 are low. The as-prepared $\alpha\text{-Fe}_2\text{O}_3@/\text{TiO}_2$ in this work shows superior cyclability and capacity compared with others summarized in **Table 1**.

EIS resistance tests are conducted for pure $\alpha\text{-Fe}_2\text{O}_3$, pure TiO_2 , and FT-1h, and the Nyquist plots of FT-1h, pure $\alpha\text{-Fe}_2\text{O}_3$, and pure TiO_2 are shown in **Figure 11D**. All of them exhibit a similar profile. There is a depressed semicircle in the high-frequency region and an inclined line in the low-frequency region. The diameter of the semicircle in the high-frequency region of each cell is related to the tenable resistance of the electrolyte (R_e), SEI layer (R_s), and charge transfer resistance (R_{ct}) (Wang et al., 2020). R_{ct} is associated with the transfer of electrons and Li^+ . The inclined line in the low-frequency region represents the Warburg impedance (Z_w), which is derived from lithium-ion diffusion in electrode materials. A semicircle with a larger diameter in the high-frequency region represents a larger R_{ct} (Yang et al., 2019). From **Figure 11D**, it can be found that the impedance of $\alpha\text{-Fe}_2\text{O}_3$ alone is relatively large, and the impedance decreases after coating with TiO_2 , indicating that the electrical conductivity of the electrode is improved by forming a composite material. In addition, the higher slope of FT-1h compared with pure $\alpha\text{-Fe}_2\text{O}_3$ in the low-frequency region is evidence of a stronger interaction between Li ions and FT-1h.

CONCLUSION

In summary, the volume expansion rates of $\alpha\text{-Fe}_2\text{O}_3$ and TiO_2 during Li-ion insertion were estimated through DFT calculations. The expansion rate of $\alpha\text{-Fe}_2\text{O}_3$ with Li-ion insertion is clearly higher than that of TiO_2 , indicating that TiO_2 could effectively alleviate crystal expansion when used in Li-ion batteries. Hence, to buffer the bulk expansion of $\alpha\text{-Fe}_2\text{O}_3$ that occurs during the discharge/charge process, cubic $\alpha\text{-Fe}_2\text{O}_3$ was coated with a TiO_2 layer ($\alpha\text{-Fe}_2\text{O}_3@/\text{TiO}_2$) using the hydrothermal method, and then a buffer chamber was deliberately designed by immersing in hydrochloric acid for etching. It is found that $\alpha\text{-Fe}_2\text{O}_3@/\text{TiO}_2$ with a buffer chamber structure could effectively relieve the volume expansion. Due to these structural advantages, the optimized FT-1h sample exhibits high reversible capacities of 1,489.3, 586.8, 438.7, 332.7, and 224.5 mA h g^{-1} at 100 mA g^{-1} , 200 mA g^{-1} , 500 mA g^{-1} , 1 A g^{-1} , and 2 A g^{-1} , respectively. When the current density is returned to 100 mA g^{-1} , the reversible capacity remains unchanged at 555.5 mA h g^{-1} . Thanks to the buffer chambers, FT-1h demonstrates good cycling performance. After 150 charge–discharge cycles at a current

density of 100 mA g^{-1} , the reversible capacity is 893.7 mA h g^{-1} , the Coulombic efficiency is 98.4%, and the morphology is in a good condition. Furthermore, the results obtained in this study provide new insights into the synthesis of metal oxide-based LIB anode materials with well-designed structures.

DATA AVAILABILITY STATEMENT

The original contributions presented in the study are included in the article/**Supplementary Material**, and further inquiries can be directed to the corresponding authors.

AUTHOR CONTRIBUTIONS

BW, BN, and DW designed the calculations and experiments. HR and CM performed the material synthesis, characterization, and battery tests. CP and WP analyzed the data and drafted the manuscript. XC, LZ, JL, and XS conducted the calculation. YS and RT made the major revision. All authors participated in discussions.

FUNDING

This work was financially supported by the National Nature Science Foundation of China (No. U1904198), the Science and Technology Department of Henan Province (No. 202102210001), the Natural Science Foundation of Henan Province (No. 202300410015), the Key Scientific Research Project of Higher Education of Henan Province (No. 20B140012), and the Ninth Group of Key Disciplines in Henan Province (No. 2018119).

SUPPLEMENTARY MATERIAL

The Supplementary Material for this article can be found online at: <https://www.frontiersin.org/articles/10.3389/fchem.2022.866369/full#supplementary-material>

Supplementary Figure S1 | Unit cells of $\alpha\text{-Fe}_2\text{O}_3$ (A) and TiO_2 (B).

Supplementary Figure S2 | XRD of $\alpha\text{-Fe}_2\text{O}_3$.

Supplementary Figure S3 | SEM images of pure Fe_2O_3 (A,B) and FT-1h (C,D) after 100 charge–discharge cycles.

Supplementary Table S1 | Data compared with other theoretical and experimental data for $\alpha\text{-Fe}_2\text{O}_3$ and TiO_2 .

Supplementary Table S2 | Volume (V) and expansion rate (E_v) of the one, two, three, four, and five and one, second, and three Li ions inserted in the cell at different sites of $\alpha\text{-Fe}_2\text{O}_3$ and TiO_2 .

Supplementary Table S3 | Electronic population of Fe-O and Ti-O bonds for $\alpha\text{-Fe}_2\text{O}_3$ and TiO_2 with and without Li inserted at symmetrical sites.

Supplementary Table S4 | Average core–shell size of oxalic acid-treated $\alpha\text{-Fe}_2\text{O}_3$ coated with TiO_2 and etched for different periods of time (FT-0.5h (A-C), FT-2h (D-F), FT-4h (G-I), and FT-12h (J-L) (pure TiO_2)).

REFERENCES

- Aouadi, S. M. (2006). Structural and Mechanical Properties of TaZrN Films: Experimental and Ab Initio Studies. *J. Appl. Phys.* 99, 053507. doi:10.1063/1.2178394
- Arlt, T., Bermejo, M., Blanco, M. A., Gerward, L., Jiang, J. Z., Staun Olsen, J., et al. (2000). High-pressure Polymorphs of anataseTiO₂. *Phys. Rev. B* 61, 14414–14419. doi:10.1103/physrevb.61.14414
- Chen, Y., Liang, J., Tian, Q., Zhang, W., and Sui, Z. (2020). Facile Construction of Clustered Fe₂O₃/TiO₂ Composite for Improved Lithium Storage Performance. *Synth. Met.* 263, 116353. doi:10.1016/j.synthmet.2020.116353
- Dufferer, F., Kronemeyer, N., Tübke, J., Leher, J., Winter, M., and Schmich, R. (2021). Post-lithium-ion Battery Cell Production and its Compatibility with Lithium-Ion Cell Production Infrastructure. *Nat. Energ.* 6, 123–134. doi:10.1038/s41560-020-00748-8
- Fan, Y., Chen, X., Zhang, K., Rong, J., and Yu, X. (2021). A Coordinated Regulation Strategy to Improve Electronic Conductivity and Li-Ion Transport for TiO₂ Lithium Battery Anode Materials. *J. Alloys Compd.* 860, 158282. doi:10.1016/j.jallcom.2020.158282
- Finger, L. W., and Hazen, R. M. (1980). Crystal Structure and Isothermal Compression of Fe₂O₃, Cr₂O₃, and V₂O₃ to 50 Kbars. *J. Appl. Phys.* 51, 5362. doi:10.1063/1.327451
- Fu, Y., Wei, Q., Wang, X., Shu, H., Yang, X., and Sun, S. (2015). Porous Hollow α -Fe₂O₃@TiO₂ Core-Shell Nanospheres for superior Lithium/sodium Storage Capability. *J. Mater. Chem. A* 3, 13807–13818. doi:10.1039/c5ta02994e
- Gao, Y., Wang, C., Hu, P., He, F., Wu, M., and Zhang, H. (2019). Carbon-incorporated, Nitrogen-Doped branch-like TiO₂ Nanostructure towards superior Lithium Storage Performance. *J. Alloys Compd.* 787, 944–951. doi:10.1016/j.jallcom.2019.02.169
- Guo, M., and Li, H. (2021). The Hydrolyzed Mil-88B(Fe) with Improved Surface Area for High-Capacity Lithium Ion Battery. *Front. Energ. Res.* 9, 781008. doi:10.3389/fenrg.2021.781008
- Hohenberg, P. (1964). Inhomogeneous Electron Gas. *Phys. Rev.* 136, B864–B871. doi:10.1103/physrev.136.b864
- Huo, J., Ren, Y., Xue, Y., Liu, Y., and Guo, S. (2021). Sulfur/nitrogen Dual-Doped Three-Dimensional Reduced Graphene Oxide Modified with Mesoporous TiO₂ Nanoparticles for Promising Lithium-Ion Battery Anodes. *J. Alloys Compd.* 868, 159183. doi:10.1016/j.jallcom.2021.159183
- Jenness, G. R., Seiter, J., and Shukla, M. K. (2018). DFT Investigation on the Adsorption of Munition Compounds on α -Fe₂O₃: Similarity and Differences with α -Al₂O₃. *Phys. Chem. Chem. Phys.* 20, 18850–18861. doi:10.1039/c8cp02590h
- Jin, L., Yuan, J., Shellikeri, A., Naderi, R., Qin, N., Lu, Y., et al. (2021). An Overview on Design Parameters of Practical Lithium-Ion Capacitors. *Batteries & Supercaps* 4, 749–757. doi:10.1002/batt.202000296
- Kaprans, K., Mateuss, J., Dorondo, A., Bajars, G., Kucinskis, G., Lesnicens, P., et al. (2018). Electrophoretically Deposited α -Fe₂O₃ and TiO₂ Composite Anchored on rGO with Excellent Cycle Performance as Anode for Lithium Ion Batteries. *Solid State Ionics* 319, 1–6. doi:10.1016/j.ssi.2018.01.042
- Kim, T., Song, W., Son, D.-Y., Ono, L. K., and Qi, Y. (2019). Lithium-ion Batteries: Outlook on Present, Future, and Hybridized Technologies. *J. Mater. Chem. A* 7, 2942–2964. doi:10.1039/c8ta10513h
- Kohn, W., and Sham, L. J. (1965). Self-Consistent Equations Including Exchange and Correlation Effects. *Phys. Rev.* 140, A1133–A1138. doi:10.1103/physrev.140.a1133
- Kong, D., Cheng, C., Wang, Y., Liu, B., Huang, Z., and Yang, H. Y. (2016). Seed-assisted Growth of α -Fe₂O₃ Nanorod Arrays on Reduced Graphene Oxide: a superior Anode for High-Performance Li-Ion and Na-Ion Batteries. *J. Mater. Chem. A* 4, 11800–11811. doi:10.1039/c6ta04370d
- Li, H., Hu, Z., Xia, Q., Zhang, H., Li, Z., Wang, H., et al. (2021a). Operando Magnetometry Probing the Charge Storage Mechanism of CoO Lithium-Ion Batteries. *Adv. Mater.* 33, 2006629. doi:10.1002/adma.202006629
- Li, H., Wang, Y., Chen, H., Niu, B., Zhang, W., and Wu, D. (2021). Synergistic Mediation of Polysulfide Immobilization and Conversion by a Catalytic and Dual-Adsorptive System for High Performance Lithium-Sulfur Batteries. *Chem. Eng. J.* 406, 126802. doi:10.1016/j.cej.2020.126802
- Li, H., Wu, L.-J., Zhang, S.-G., Yao, C., Chao, C.-Y., Yue, H.-W., et al. (2020). Facile Synthesis of Mesoporous One-Dimensional Fe₂O₃ Nanowires as Anode for Lithium Ion Batteries. *J. Alloys Compd.* 832, 155008. doi:10.1016/j.jallcom.2020.155008
- Li, J., Wang, N., Deng, J., Qian, W., and Chu, W. (2018). Flexible Metal-Templated Fabrication of Mesoporous Onion-like Carbon and Fe₂O₃@N-Doped Carbon Foam for Electrochemical Energy Storage. *J. Mater. Chem. A* 6, 13012–13020. doi:10.1039/c8ta02417k
- Li, Q., Li, H., Xia, Q., Hu, Z., Zhu, Y., Yan, S., et al. (2021b). Extra Storage Capacity in Transition Metal Oxide Lithium-Ion Batteries Revealed by *In Situ* Magnetometry. *Nat. Mater.* 20, 76–83. doi:10.1038/s41563-020-0756-y
- Li, S., Zhang, Y., and Huang, J. (2019a). Three-dimensional TiO₂ Nanotubes Immobilized with Fe₂O₃ Nanoparticles as an Anode Material for Lithium-Ion Batteries. *J. Alloys Compd.* 783, 793–800. doi:10.1016/j.jallcom.2018.12.371
- Li, Z., Mao, Y., Tian, Q., Zhang, W., and Yang, L. (2019b). Extremely Facile Preparation of High-Performance Fe₂O₃ Anode for Lithium-Ion Batteries. *J. Alloys Compd.* 784, 125–133. doi:10.1016/j.jallcom.2018.12.392
- Liang, Y., Xiong, X., Xu, Z., Xia, Q., Wan, L., Liu, R., et al. (2020). Ultrathin 2D Mesoporous TiO₂/rGO Heterostructure for High-Performance Lithium Storage. *Small* 16, e2000030. doi:10.1002/sml.202000030
- Monkhorst, H. J., and Pack, J. D. (1976). Special Points for Brillouin-Zone Integrations. *Phys. Rev. B* 13, 5188–5192. doi:10.1103/physrevb.13.5188
- Narsimulu, D., Nagaraju, G., Sekhar, S. C., Ramulu, B., and Yu, J. S. (2019). Designed Lamination of Binder-free Flexible Iron Oxide/carbon Cloth as High Capacity and Stable Anode Material for Lithium-Ion Batteries. *Appl. Surf. Sci.* 497, 143795. doi:10.1016/j.apsusc.2019.143795
- Ni, L., Wang, R., Fu, Y., Wang, H., Liu, W., Zhu, L., et al. (2019). Nanoengineering Mesoporous Graphene-Based Anatase/bronze TiO₂ Heterostructures for Pseudocapacitance-Enhanced Lithium-Ion Batteries. *J. Alloys Compd.* 790, 683–692. doi:10.1016/j.jallcom.2019.03.237
- Nong, S., Dong, C., Wang, Y., and Huang, F. (2020). Constructing Porous TiO₂ Crystals by an Etching Process for Long-Life Lithium Ion Batteries. *Nanoscale* 12, 18429–18436. doi:10.1039/d0nr04861e
- Perdew, J. P., Burke, K., and Ernzerhof, M. (1996). Generalized Gradient Approximation Made Simple. *Phys. Rev. Lett.* 77, 3865–3868. doi:10.1103/physrevlett.77.3865
- Perdew, J. P., Burke, K., and Ernzerhof, M. (1998). Perdew, Burke, and Ernzerhof Reply. *Phys. Rev. Lett.* 80, 891. doi:10.1103/physrevlett.80.891
- Qi, C., Liu, C., Meng, K., Yu, X., Zhang, Y., Liu, J., et al. (2018). Enhanced Performance of TiO₂/ α -Fe₂O₃ Nanostructure as Anode Material for Lithium-Ion Batteries. *Int. J. Electrochem. Sci.* 13, 265–274. doi:10.20964/2018.01.34
- Qin, G., Zeng, M., Wu, X., Wen, J., and Li, J. (2018). Fabrication of Fe₂O₃@TiO₂ Core-Shell Nanospheres as Anode Materials for Lithium-Ion Batteries. *J. Mater. Sci. Mater. Electron.* 29, 12944–12950. doi:10.1007/s10854-018-9414-4
- Qu, D., Sun, Z., Gan, S., Gao, L., Song, Z., Kong, H., et al. (2020). Two-dimensional Fe₂O₃/TiO₂ Composite Nanoplates with Improved Lithium Storage Properties as Anodic Materials for Lithium-Ion Full Cells. *ChemElectroChem* 7, 4963–4970. doi:10.1002/celec.202001143
- Shi, T., Duan, Y., Lv, K., Hu, Z., Li, Q., Li, M., et al. (2018). Photocatalytic Oxidation of Acetone over High Thermally Stable TiO₂ Nanosheets with Exposed (001) Facets. *Front. Chem.* 6, 175. doi:10.3389/fchem.2018.00175
- Wang, H., Wu, D., Wu, W., Wang, D., Gao, Z., Xu, F., et al. (2019a). Preparation of TiO₂ Microspheres with Tunable Pore and Chamber Size for Fast Gaseous Diffusion in Photoreduction of CO₂ under Simulated Sunlight. *J. Colloid Interf. Sci.* 539, 194–202. doi:10.1016/j.jcis.2018.12.022
- Wang, H., Wu, D., Yang, C., Lu, H., Gao, Z., Xu, F., et al. (2019b). Multi-functional Amorphous TiO₂ Layer on ZIF-67 for Enhanced CO₂ Photoreduction Performances under Visible Light. *J. CO₂ Utilization* 34, 411–421. doi:10.1016/j.jcou.2019.07.011
- Wang, H., Zhao, L., Zhang, H., Liu, Y., Yang, L., Li, F., et al. (2022). Revealing the Multiple Cathodic and Anodic Involved Charge Storage Mechanism in an FeSe₂ Cathode for Aluminium-Ion Batteries by *In Situ* Magnetometry. *Energy Environ. Sci.* 15, 311–319. doi:10.1039/d1ee03070a
- Wang, L., Wu, D., Guo, Z., Yan, J., Hu, Y., Chang, Z., et al. (2018a). Ultra-thin TiO₂ Sheets with Rich Surface Disorders for Enhanced Photocatalytic Performance under Simulated Sunlight. *J. Alloys Compd.* 745, 26–32. doi:10.1016/j.jallcom.2018.02.070
- Wang, T., Guo, W., Wang, G., Wang, H., Bai, J., and Wang, B. (2020). Highly Dispersed FeSe₂ Nanoparticles in Porous Carbon Nanofibers as Advanced

- Anodes for Sodium and Potassium Ion Batteries. *J. Alloys Compd.* 834, 155265. doi:10.1016/j.jallcom.2020.155265
- Wang, Z., Zhang, Z., Xia, J., Wang, W., Sun, S., Liu, L., et al. (2018b). Fe₂O₃@C Core@shell Nanotubes: Porous Fe₂O₃ Nanotubes Derived from MIL-88A as Cores and Carbon as Shells for High Power Lithium Ion Batteries. *J. Alloys Compd.* 769, 969–976. doi:10.1016/j.jallcom.2018.08.081
- Wu, D., Wang, X., An, Y., Song, X., Liu, N., Wang, H., et al. (2017). Hierarchical TiO₂ Structures Derived from F⁻ Mediated Oriented Assembly as Triple-Functional Photoanode Material for Improved Performances in CdS/CdSe Sensitized Solar Cells. *Electrochimica Acta* 248, 79–89. doi:10.1016/j.electacta.2017.06.150
- Xu, F., Mei, J., Zheng, M., Bai, D., Wu, D., Gao, Z., et al. (2017). Au Nanoparticles Modified Branched TiO₂ Nanorod Array Arranged with Ultrathin Nanorods for Enhanced Photoelectrochemical Water Splitting. *J. Alloys Compd.* 693, 1124–1132. doi:10.1016/j.jallcom.2016.09.273
- Yan, X., Jiang, F., Sun, X., Du, R., Zhang, M., Kang, L., et al. (2020). A Simple, Low-Cost and Scale-Up Synthesis Strategy of Spherical-graphite/Fe₂O₃ Composites as High-Performance Anode Materials for Half/full Lithium Ion Batteries. *J. Alloys Compd.* 822, 153719. doi:10.1016/j.jallcom.2020.153719
- Yang, Y., Liu, Q., Cao, M., Ju, Q., Wang, H., Fu, R., et al. (2019). Enhanced Electrochemical Performance of α -Fe₂O₃ Grains Grafted onto TiO₂-Carbon Nanofibers via a Vapor-Solid Reaction as Anode Materials for Li-Ion Batteries. *Appl. Surf. Sci.* 463, 322–330. doi:10.1016/j.apsusc.2018.08.171
- Yuan, Y. F., Chen, F., Ye, L. W., Cai, G. S., Zhu, M., Yin, S. M., et al. (2019). Construction of Co₃O₄@TiO₂ Heterogeneous Mesoporous Hollow Nanocage-In-Nanocage from Metal-Organic Frameworks with Enhanced Lithium Storage Properties. *J. Alloys Compd.* 790, 814–821. doi:10.1016/j.jallcom.2019.03.255
- Yuan, Y. F., Chen, Q., Zhu, M., Cai, G. S., and Guo, S. Y. (2021). Nano Tube-In-Tube CNT@void@TiO₂@C with Excellent Ultrahigh Rate Capability and Long Cycling Stability for Lithium Ion Storage. *J. Alloys Compd.* 851, 156795. doi:10.1016/j.jallcom.2020.156795
- Zhang, G., Shi, Y., Wang, H., Jiang, L., Yu, X., Jing, S., et al. (2019). A Facile Route to Achieve Ultrafine Fe₂O₃ Nanorods Anchored on Graphene Oxide for Application in Lithium-Ion Battery. *J. Power Sourc.* 416, 118–124. doi:10.1016/j.jpowsour.2019.01.091
- Zhang, H.-X., Zhu, Y. F., and Zhao, M. (2017). Interface Charge Transfer and Enhanced Visible Light Response of Graphene/anatase TiO₂ (110) Systems with and without Oxygen Vacancy: A DFT+U Calculation. *Appl. Surf. Sci.* 420, 105–109. doi:10.1016/j.apsusc.2017.05.142
- Zhao, W., Fei, P., Zhang, X., Zhang, Y., Qin, C., and Wang, Z. (2018). Porous TiO₂/Fe₂O₃ Nanoplate Composites Prepared by De-alloying Method for Li-Ion Batteries. *Mater. Lett.* 211, 254–257. doi:10.1016/j.matlet.2017.10.019
- Zhong, Y., Ma, Y., Guo, Q., Liu, J., Wang, Y., Yang, M., et al. (2017). Controllable Synthesis of TiO₂@Fe₂O₃ Core-Shell Nanotube Arrays with Double-Wall Coating as Superb Lithium-Ion Battery Anodes. *Sci. Rep.* 7, 40927. doi:10.1038/srep40927
- Zhu, W., Wang, Y., Yu, Y., Hu, Y., and Chen, Y. (2020). Core-shell Structured α -Fe₂O₃@Li₄Ti₅O₁₂ Composite as Anode Materials for High-Performance Lithium-Ion Batteries. *J. Alloys Compd.* 813, 152175. doi:10.1016/j.jallcom.2019.152175
- Conflict of Interest:** The authors declare that the research was conducted in the absence of any commercial or financial relationships that could be construed as a potential conflict of interest.
- Publisher's Note:** All claims expressed in this article are solely those of the authors and do not necessarily represent those of their affiliated organizations, or those of the publisher, the editors, and the reviewers. Any product that may be evaluated in this article, or claim that may be made by its manufacturer, is not guaranteed or endorsed by the publisher.
- Copyright © 2022 Pian, Peng, Ren, Ma, Su, Ti, Chen, Zhu, Liu, Sun, Wang, Niu and Wu. This is an open-access article distributed under the terms of the Creative Commons Attribution License (CC BY). The use, distribution or reproduction in other forums is permitted, provided the original author(s) and the copyright owner(s) are credited and that the original publication in this journal is cited, in accordance with accepted academic practice. No use, distribution or reproduction is permitted which does not comply with these terms.